Hyperfine structure study of ^{97,98,99}Tc in a new laser ion source for high-resolution laser spectroscopy

T. Kron,[1,2] R. Beerwerth,[3,4] S. Raeder,[2,5,*] S. Fritzsche,[3,4] R. Heinke,[1] P. Schönberg,[6] M. Trümper,[1] and K. Wendt[1]

[1]*Institute of Physics, Johannes Gutenberg University Mainz, Staudinger Weg 7, 55128 Mainz, Germany*
[2]*GSI Helmholtzzentrum für Schwerionenforschung, Planckstrasse 1, 64291 Darmstadt, Germany*
[3]*Helmholtz-Institut Jena, Fröbelstieg 3, 07743 Jena, Germany*
[4]*Theoretisch-Physikalisches Institut, Friedrich-Schiller-Universität Jena, Fröbelstieg 1, 07743 Jena, Germany*
[5]*Helmholtz-Institut Mainz, Staudingerweg 18, 55128 Mainz, Germany*
[6]*Institute of Nuclear Chemistry, Johannes Gutenberg University Mainz, Fritz-Straßmann-Weg 2, 55128 Mainz, Germany*

(Received 13 March 2020; accepted 2 July 2020; published 3 September 2020)

Using a novel concept for efficient laser spectroscopy, we investigated the hyperfine splittings of three different atomic transitions in the long-lived isotopes $^{97-99}$Tc. Despite the refractory character of the element technetium, sample sizes as low as 10^{11} atoms were sufficient to achieve excellent signal-to-noise ratios at a spectroscopic linewidth of less than 100 MHz. The obtained spectra were analyzed in detail, which results in a very good consistency for the extracted hyperfine parameters from the different transitions. The presented measurements provide the first hyperfine structure data for the isotopes ^{97,98}Tc from which, in combination with the known nuclear moments of ^{99}Tc, their nuclear magnetic dipole and electric quadrupole moments were extracted. In addition, the experimental data confirm the predicted nuclear spin of ^{98}Tc to $I = 6$. In combination with atomic Multiconfiguration Dirac-Hartree-Fock calculations, the observed isotope shifts were investigated and the changes in mean-square charge radii were determined.

DOI: 10.1103/PhysRevC.102.034307

I. INTRODUCTION

Technetium ($Z = 43$) is the lightest element with exclusively radioactive isotopes. Although located in the middle of the periodic table, it was discovered only in 1937 after irradiating a molybdenum sample with a deuterium beam [1]. The half-lives of the three most long-lived isotopes, ^{97}Tc, ^{98}Tc, and ^{99g}Tc, are 4.2×10^6, 4.2×10^6, and 2.1×10^5 yr, respectively. Only minor traces of the isotope ^{99g}Tc occur naturally, primarily from the spontaneous fission of ^{238}U. The main portion of the technetium detected worldwide today was produced anthropologically in neutron-induced fission of ^{235}U in nuclear reactors. Here, ^{99g}Tc features a fission yield of about 6%, and therefore technetium poses a substantial amount of the long-lived nuclear waste. The nuclear structure of the isotopes around ^{99}Tc are located just above the $Z = 40$ and $N = 50$ shell closures, and investigations on the shape and deformation of these nuclei will therefore advance the understanding of the transition from spherical nuclei to well-deformed nuclei [2,3]. Investigations of the nuclear level structure in this region indicate a rather sudden transition to an axial-deformed rotor around $N = 60$ while the nuclides with lower neutron numbers are γ-unstable rotors [4], and, in addition, ^{98}Mo shows the evidence for shape coexistence [5,6]. So far, the refractory character of the transition metal technetium, as well as the limited information on the atomic structure impeded laser spectroscopic investigations of Tc isotopes, especially at isotope separator on-line (ISOL) facilities.

The atomic level structure of ^{99}Tc was investigated by Bozman *et al.* [7] and by Palmeri and Wyart [8]. In several low-lying multiplets the hyperfine structure (HFS) was partly resolved and investigated by Wendlandt *et al.* [9], but only for the isotope ^{99}Tc. Similarly, for the long-lived isotopes the nuclear magnetic dipole moment was studied only for ^{99}Tc by different techniques [9–12], while the most accurate value of $\mu(^{99}\text{Tc}) = 5.6847(4)\,\mu_N$ is based on nuclear magnetic resonance (NMR) measurements by Walchli *et al.* [10]. Additional measurements on nuclear moments exist for the shorter-lived isotopes $^{93-96}$Tc by NMR on oriented nuclei [13]. The spectroscopic electric quadrupole moment for ^{99}Tc was measured to be $Q_s = -0.129(6)$ eb [14] which is the only reported value for any Tc isotope. This quadrupole moment disagrees with some (positive) values in Refs. [9,12], but its magnitude is supported by [15] using *ab initio* calculations and is currently considered to be the most accurate value [16]. A nuclear spin of $I = 9/2$ is confirmed for the isotopes ^{97}Tc and ^{99}Tc, while the spin of ^{98}Tc could not be identified uniquely so far, although a value of $I = 6$ has been suggested [17]. In a preparatory experiment, we investigated the HFS in transitions of the odd-mass isotopes ^{97}Tc and ^{99}Tc with resonance ionization spectroscopy (RIS) [18], while in this work the measurement and evaluation were refined using three different

*s.raeder@gsi.de

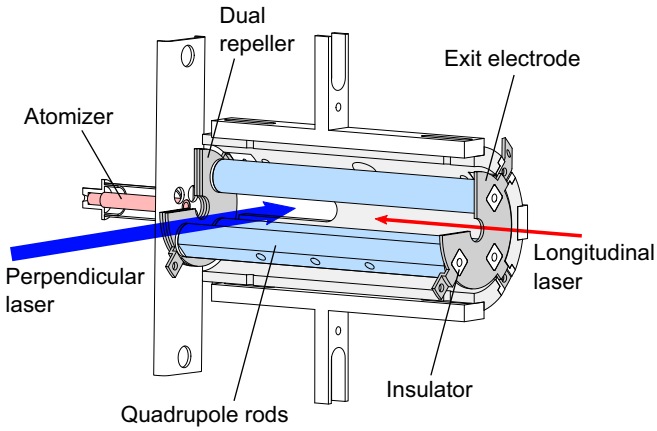

FIG. 1. Sectional view of the PI-LIST, which enables longitudinal (red arrow) and perpendicular (blue arrow) laser irradiation and interaction.

optical transitions. In addition, the isotope ^{98}Tc was investigated laser spectroscopically for the first time. Besides the information of the nuclear properties of the technetium isotopes, the presented results foster the current Tc trace analysis project at Mainz University [19–21], where the spectroscopic information on ^{97}Tc is essential for using this isotope as tracer.

II. EXPERIMENTAL SETUP

The resonance ionization spectroscopy (RIS) experiments presented here were performed at the RISIKO mass separator at Mainz university. This off-line separator is similar to the ISOLDE on-line isotope separator at CERN [22] and is regularly used for technical development of new devices and techniques at the laser ion source or ion detection components. It comprises a hot cavity atomizer/ion source from which the created ions are accelerated to 30 keV, mass separated by a 60° sector field magnet, and finally detected using a secondary electron multiplier for single-ion detection. For this setup total efficiencies with laser ionization of up to 54% were demonstrated, including sample atomization, laser ionization, separator transmission, and ion-detection efficiency [23,24].

The key device for the present experiment was the newly developed perpendicularly illuminated laser ion source and trap (PI-LIST) as shown in Fig. 1. It is based on the LIST device [25–28] but offers perpendicular laser access to the atomic beam emerging from the resistively heated atomizer. Furthermore, it employs a dual repeller to suppress the ionic background caused by surface ionization from the hot atomizer as well as interfering electron impact ionization from electrons that are accelerated in electric stray fields. The perpendicular orientation of the laser radiation and the atomic beam leads to a significant reduction of the thermal Doppler broadening from about 3 GHz down into the 100-MHz region.[1] The ionization region is located inside a radio-frequency quadrupole structure that ensures transversal confinement of the generated ions for optimum transportation efficiency through the PI-LIST and prevents influences from the strong acceleration field into the laser-atom interaction region. More details and technical aspects of the PI-LIST are given in Ref. [29].

A pulsed Ti:sapphire laser system provides the radiation for the different resonant excitation of the atomic transitions as shown in Fig. 3. Its specifications feature a high repetition rate of 10 kHz with pulse lengths of about 40 ns, a wavelength range of 690–960 nm, and a high output power of up to 4 W [30]. If required the wavelength range is extended by frequency conversion using second-, third-, and forth-order harmonic generation. This all solid-state laser system was specifically designed to meet the requirements of RIS and today has been established as a universal and reliable tool for on-line laser ion sources worldwide [31]. To produce the required laser radiation with a narrow spectral bandwidth, as applied for high-resolution spectroscopy in the first-excitation step transition, a specific frequency-doubled injection-locked Ti:sapphire laser was added. For this purpose, the Ti:sapphire laser cavity was seeded with cw radiation from a commercial, cw narrowband, external-cavity diode laser system, which was frequency locked to a stabilized HeNe laser via fringe-offset locking. The spectral bandwidth of the fundamental radiation from the pulsed injection-locked Ti:sapphire laser at 848–860 nm is about 10–20 MHz, close to the Fourier-limit given by the laser pulse duration. The frequencies of all lasers were recorded using a wavemeter (WSU, High Finesse), which was regularly calibrated to the stabilized HeNe laser. More technical details on this system can be found in Refs. [32,33].

III. EXPERIMENTAL RESULTS

In the experiment, samples with about 10^{11}–10^{13} atoms of Tc were used for the spectroscopic investigations which correspond to an activity of the sample below 10 Bq for all isotopes under study. Careful optimization of the experimental system was obtained by laser ionization initially using broad-bandwidth laser radiation inside the hot cavity and in the ion guide mode of the LIST where all ions created inside the atomizer and inside the RFQ structure are extracted. In a second step afterwards the ions were created in normal LIST mode where the lasers are still arranged anticollinearly to the atom beam but with suppression of ions from the atomizer before finally switching to perpendicular illumination. In this way, a signal-to-background ratio of more than 1000 was achieved, as can be seen in the well-resolved mass spectrum in Fig. 2. The remaining background of about 0.5 events per second is caused by the dark count rate of the ion detection and electronic noise contributions. The overall efficiency achieved within the RIS experiment in Tc was estimated to be of the order of 10^{-4} in the case of broad-bandwidth laser excitation in the PI-LIST. Depending on the HFS structure, the efficiency of the ionization scheme, and the laser power, this value is significantly reduced to an estimated value of about 10^{-6}. A more detailed discussion on this aspect is given in Ref. [29].

In total, three first transitions with different angular momenta J of the excited, upper atomic level, as summarized

[1]Throughout the article spectral widths are considered in full width at half maximum if not noted otherwise.

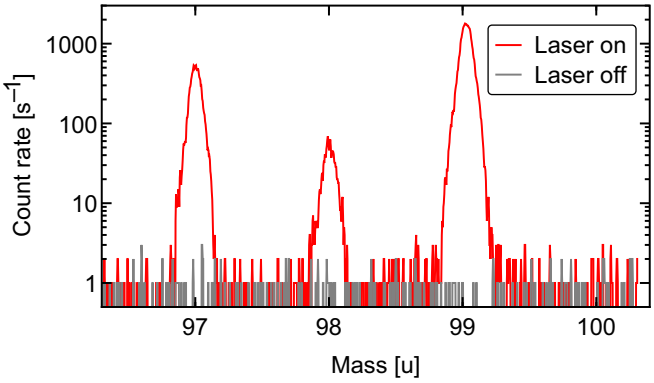

FIG. 2. Mass spectrum in the Tc region measured at the RISIKO mass separator using the PI-LIST with longitudinal laser alignment.

in Fig. 3, were investigated with high resolution. Due to the interaction with the nuclear spin I the atomic levels split into hyperfine components with specific quantum numbers $|I - J| < F < I + J$, resulting in up to 18 individual hyperfine transitions. As an example, Fig. 4 shows the spectra of the transition from the $4d^5\,5s^2\,{}^6S_{5/2}$ ground state to the $4d^5\,5s\,5p\,{}^6P^o_{7/2}$ state centered at 23 265.32 cm^{-1}, corresponding to a wavelength of about 430 nm, for all three isotopes under study. Here all expected 18 individual transitions are fully resolved, arranged in four triplets, two doublets, and two singlets. The individual HFS multiplets were scanned multiple times with a frequency step width of 10 MHz for the scanning laser, while the count rate and the laser frequency from the wavemeter were recorded. For further evaluation, the data sets of all individual scan sections of one spectrum were combined and binned in intervals of 10 MHz in width.

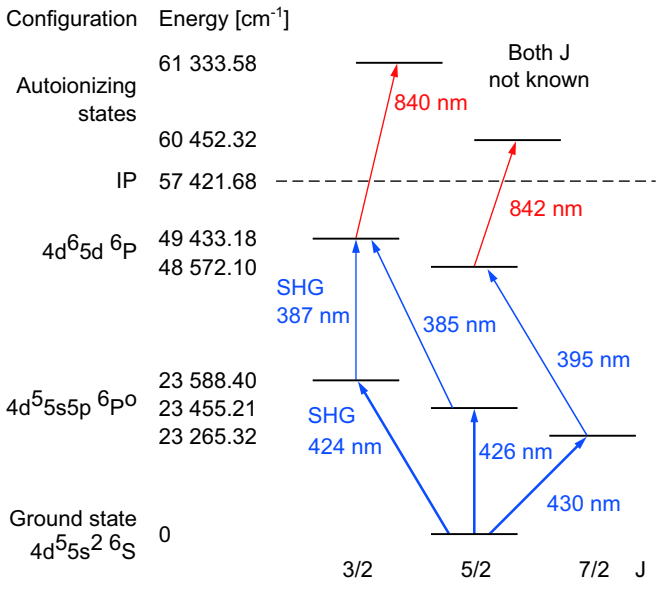

FIG. 3. Three-step ionization schemes in Tc used for the investigations in this work. Levels are arranged according to their total angular moment J, as given below the schemes.

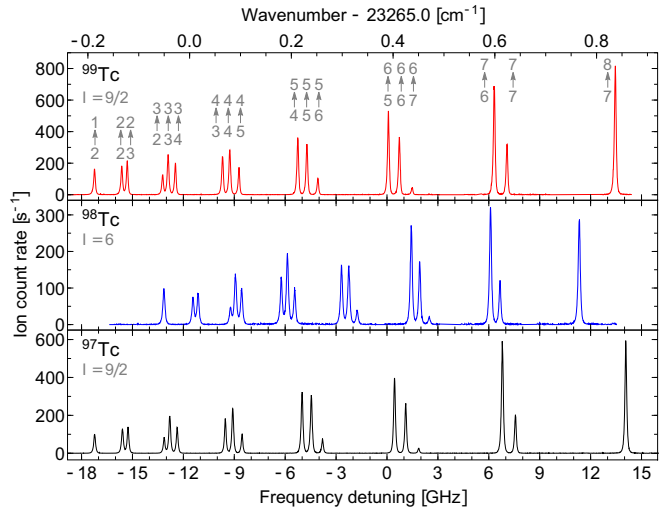

FIG. 4. Experimental HFS structure of the $J = 5/2$-$J' = 7/2$ transition at 430 nm in Tc. The data were binned to intervals of 10 MHz in width. The frequency axis is given relative to 23 265.388 cm^{-1}, the center of gravity for the HFS of ^{97}Tc. The associated F-F' transitions are indicated in gray in the ^{99}Tc spectrum.

In these measurements, the laser power for the first and second steps was lowered down to 0.5 and 6.0 mW, respectively, to suppress power broadening. In addition, a temporal delay of about 40 ns between the laser pulses of these interconnected excitation steps was applied to minimize power broadening effects induced by the coupling to the second excitation step [34–37]. To nevertheless ensure optimal ionization conditions, the third-step laser was set to its maximum power of 2500 mW.

An average spectral linewidth of 124 MHz was achieved, ranging down to only 98 MHz under optimal conditions, i.e., at low oven temperatures and with the lowest laser power. All individual transitions in the spectra can be clearly identified and a sum of Voigt profiles was fitted to each spectrum. While the Gaussian contributes on average about 82 MHz to the width, the Lorentzian component contributes just 58 MHz. A closer look at the effects involved in the ionization process can give additional information on the PI-LIST performance and its influence on the data. We assume that the second-order harmonic laser radiation has a Gaussian-shaped spectral profile with a spectral width of about 17 MHz, as determined in earlier measurements. The remaining Gaussian contribution is about 78 MHz and arises from the residual thermal Doppler broadening in the direction of the laser beam. This agrees well with the typical temperature of the atomizer of about 1700 °C and an estimated geometric half opening angle of about 2° for atoms from the atomizer to enter the ionization volume. These assumptions are supported by the fact that the Gaussian contribution is accordingly larger for spectra taken at slightly higher temperatures needed to compensate for smaller sample sizes. The Lorentzian contribution includes both, the natural linewidth and the power broadening, which cannot be eliminated completely. Using the transition strength of 4.2×10^7 s^{-1} [8] of the excitation into the $4d^5\,5s\,5p\,{}^6P^o_{7/2}$ state, the natural linewidth is estimated to be 6.7 MHz or even

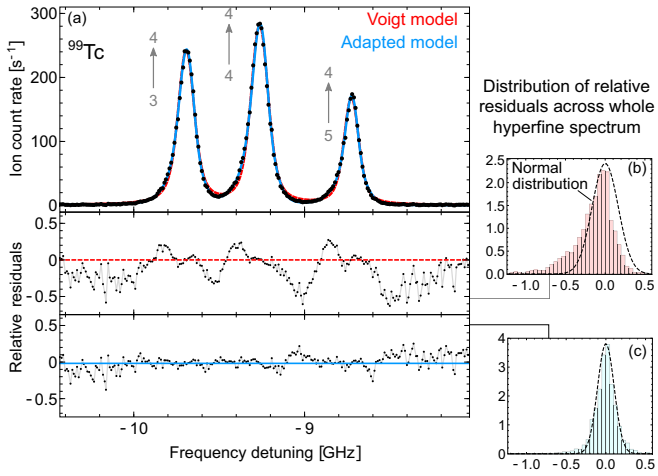

FIG. 5. Excerpt of the fitted ^{99}Tc spectrum showing the resulting curves for a fit using standard Voigt profiles (dashed red line) and asymmetric Bi-Voigt profiles (solid blue line) for each resonance [panel (a)]. The lower section shows the residuals relative to the y value of each point. Panels (b) and (c) show the corresponding distribution of the residuals across the whole hyperfine spectrum. See text for further explanation.

slightly larger if any unknown but sufficiently strong additional decay channels may exist. As a result, the remaining power broadening in the different spectra can be estimated to be about 20–60 MHz.

The Voigt fit matches the experimental data well, but a small systematic discrepancy was found in the spectra when examined in detail. As an example, Fig. 5(a) shows the Voigt model fit as a dashed, red line and the corresponding residuals in the lower section. Two different systematic peculiarities can be observed: The experimental data show a slight asymmetry, and the fitted curve lies above the experimental data on all tailings further off the resonance center. However, this can be explained by specific aspects of the ionization process and will be considered in the fit model later on.

The asymmetry in the hyperfine spectra can be caused by two effects. The first one is the inaccuracy in the alignment of the exciting laser beam relative to the central axis of the atomic beam, which might lead to an anisotropic particle density and atom velocity distribution within the interaction region. A second contribution to the asymmetry can result from chirp effects in the exciting laser light. Here, the laser frequency is affected by the laser field intensity in the cavity and thus by changes during the temporal evolution of the laser pulse, resulting in an asymmetric line profile for the excitation process. This effect was not studied for the injection-locked Ti:sapphire laser system used here, but comparable laser systems indicate frequency variations on the order of some kHz up to a few MHz, which fits to the observed frequency scale [38,39].

The mismatch in the tailing in comparison to a simple Voigt profile is expected to result from a varying power broadening during an excitation laser pulse. Although, the second and third laser pulses with a duration of about 45 ns were delayed by 40 ns relative to the spectroscopic excitation, a fraction of light from the first-step laser is still present at that time. This could result in a larger broadening and an impact on the tailing of the resonance [35,37]. In addition, it is expected that the spatial power distribution of the laser is not constant across the whole ionization volume and may introduce a varying power broadening.

To account for these effects, two changes were made to the fit model. First, the basic Voigt profile was modified to allow for a simple asymmetry as described in Ref. [40]. This introduced one additional fit parameter, which defined the strength and the direction of the asymmetry for all peaks in a single spectrum. Second, an additional Voigt profile with a lower peak height and an increased width was added to each resonance peak to account for the pronounced tails due to the temporal varying spectral broadening of the resonances during a laser pulse. The center and the Lorentzian width of the smaller Voigt profile were set identical to those of the associated main Voigt profile. The Gaussian width and the height ratio to the main Voigt profile were set identical for all smaller Voigt profiles in a spectrum, which introduced another two fit parameters. Figure 5(a) also includes the fitted asymmetric Bi-Voigt profile.

Although this model has only three additional fit parameters per spectrum, it matches the experimental data significantly better across the entire spectrum. As can be seen in the lower trace of Fig. 5(a) it fully eliminates the systematic deviation of the residuals as observed with the simple Voigt profiles. The corresponding histogram of the residuals' distribution for the whole hyperfine spectrum including all hyperfine transitions is given in Figs. 5(b) and 5(c). It matches a normal distribution (dashed line) for the adopted model. Furthermore, the resulting ground-state HFS parameters from the asymmetric Bi-Voigt fit scatter less across the three investigated transitions for all three Tc isotopes under study. To account for uncertainties that could be introduced by thermal drifts and systematic deviations of the wavemeter, as well as changes in the geometric overlap of atom and laser beams that are not covered by the adopted Voigt profiles, a conservative systematic uncertainty estimated from repeating HFS measurements, e.g., in Ac [41], was added on top of the errors derived by the fitting routine for each spectrum. These additional uncertainties dominate the final error and are at least 6 times larger than the standard errors from the fitting routine and about 3 times larger than the observed scatter when comparing the results for the ground state across the three investigated transitions. Nevertheless, the experimental uncertainties do not limit the extracted nuclear properties.

IV. HYPERFINE STRUCTURE

The extracted A and B hyperfine parameters obtained from the spectra are summarized in Table I. The values for the $4d^5\,5s^2\,{}^6S_{5/2}$ ground state as quoted are the weighted mean values from the data obtained in the three investigated transitions. For comparison, literature values for ^{99}Tc from Ref. [9] are listed in the last column of Table I. These agree perfectly well with our results for all three upper $4d^5\,5s\,5p\,{}^6P^o$ states, while there is a 2σ discrepancy in the ground-state A parameter, which are extracted in both experiments from the

TABLE I. Compilation of the HFS coupling constants derived from the HFS spectra in the first excitation step. The literature values for ^{99}Tc are taken from Ref. [9]. All values are given in units of MHz.

Parameter	^{97}Tc	^{98}Tc	^{99}Tc	^{99}Tc$_{\text{lit}}$
$4d^5\,5s^2\,{}^6S_{5/2}$				
A	−109.50(13)	−65.86(10)	−107.34(8)	−109.12(90)
B	1.9(44)	1.5(63)	0.3(20)	—
$4d^5\,5s\,5p\,{}^6P^o_{7/2}$				
A	815.77(42)	490.96(32)	799.99(26)	798.6(36)
B	−59.2(75)	17.0(108)	−43.9(35)	−57(18)
$4d^5\,5s\,5p\,{}^6P^o_{5/2}$				
A	911.32(45)	548.60(34)	894.08(28)	892.2(39)
B	71.3(81)	−9.4(112)	57.4(38)	93(18)
$4d^5\,5s\,5p\,{}^6P^o_{3/2}$				
A	1207.19(42)	726.85(34)	1183.27(27)	1182.1(36)
B	−6.5(72)	−3.1(105)	−12.6(34)	−12(12)

fits with extremely high precision of well below 1 per mill. In this respect, it is important to note that in the work of Wendlandt *et al.* it is stated that "the ground-level splitting could not be completely resolved" [9]. Thus, therein a not further explained "numerical profile analysis" was used to derive the corresponding A parameters, while no values for the B parameter were extracted. As discussed above and shown in Fig. 4 the ground-state splitting was perfectly resolved in the present work, which allows for conclusive determination of the HFS A and B parameters. In addition, individual A parameters agree fully across the three investigated transitions within their respective error bars. From the unresolved ground-state splitting in Ref. [9], we conclude that the uncertainty of 0.9 MHz stated therein seems to be slightly underestimated.

V. NUCLEAR MOMENTS

As the HFS is based on the interaction between the magnetic moments of the atomic electrons and the nucleus, HFS coupling constants as well as isotope-shift parameters can be used to deduce nuclear moments and shape development. The nuclear spin of ^{98}Tc had not been directly measured to date but had been predicted to be $I = 6$ [17]. Our measurements confirm $I = 6$, as for any other spin value the resonance peaks could not be fitted simultaneously to each hyperfine spectrum of ^{98}Tc.

The magnetic dipole moment μ_I is part of the hyperfine coupling constant A while the spectroscopic electric quadrupole moment Q_s of the nucleus is linked to B. The so far unknown moments μ_I and Q_s of ^{97}Tc and ^{98}Tc were calculated using the respective values of a reference isotope and the relations

$$\mu_I = \mu_I^{\text{ref}} \frac{AI}{A^{\text{ref}} I^{\text{ref}}} \quad \text{and} \quad Q_s = Q_s^{\text{ref}} \frac{B}{B^{\text{ref}}}. \tag{1}$$

In the following, we use the known moments of ^{99g}Tc as reference. Its magnetic dipole moment $\mu_{I,99} = 5.6847(4)$ in units of the nuclear magneton μ_N was precisely measured by Walchli *et al.* using a nuclear magnetic resonance technique, resulting in Refs. [10,16]. In addition, ^{99g}Tc is the only isotope with a known spectroscopic electric quadrupole moment, which was measured to be −0.129(6) eb, confirmed by *ab initio* calculations [14,15]. With these values, the moments for ^{97,98}Tc were calculated as summarized in Table II.

Formula (1) neglects any form of HFS anomaly, like the Bohr-Weisskopf effect and the Breit-Rosenthal effect, which describe the change of the atomic shell to nucleus interaction for different isotopes due to variations of the magnetization and charge distribution inside the nucleus. In the region of $Z = 43$, these effects typically cause changes well below 1% [42], which was conservatively adopted as an additional error in the determination of the magnetic moment. From the obtained magnetic dipole moments, the g factors of the nuclei can be calculated and are shown in Fig. 6. ^{97}Tc clearly follows the trend of the odd-mass isotopes where the magnetic moment corresponds to the $g_{9/2}$ shell of the unbound proton with a slight reduction of the g factor with increasing neutron number.

The nuclear magnetic moment of the odd-odd isotope ^{98}Tc with an odd number of protons ($Z = 43$) and an odd number of neutrons ($N = 55$) was measured to $\mu^{\text{exp}}(^{98}\text{Tc}) = -4.651(55)\ \mu_N$. This value is very close to the value of $\mu^{jj-\text{add}}(^{98}\text{Tc}) = -4.70\ \mu_N$ calculated using the additivity in the jj-coupling limit of the unbound proton and neutron [43] by taking the g factor for the $(\pi g_{9/2})^3$ proton configuration from the average of ^{97,99}Tc and the g factor for the $(\nu d_{5/2})^5$ neutron configuration from the average of the isotones ^{97}Mo

TABLE II. Nuclear magnetic dipole moments and spectroscopic nuclear electric quadrupole moments for the chain of Tc isotopes.

Isotope	I	μ_I (μ_N)	Q_s (eb)
Tc-99	9/2	5.6847(4)[a]	−0.129(6)[a]
Tc-98	6	4.651(55)	+0.036(24)
Tc-97	9/2	5.799(66)	−0.167(20)
Tc-96	7	5.09(5)[a]	
Tc-95	9/2	5.94(6)[a]	
Tc-94	7	5.12(5)[a]	
Tc-93	9/2	6.32(6)[a]	

[a]Literature value taken from Ref. [16].

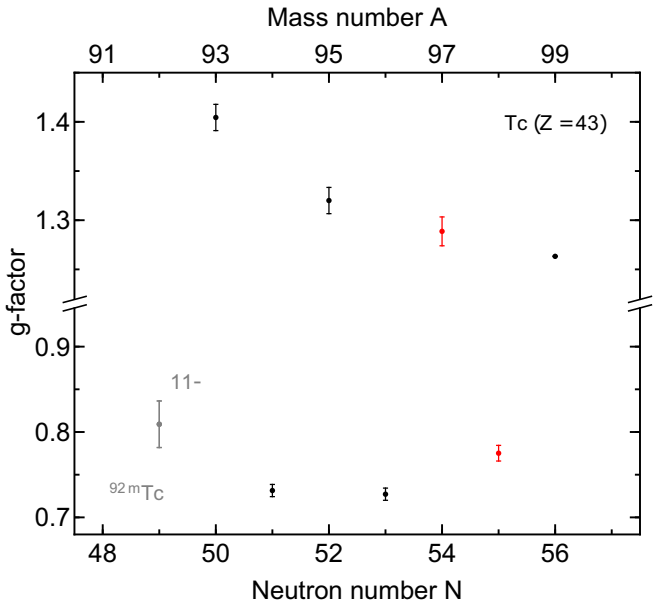

FIG. 6. Nuclear g factor in the Tc isotope chain. The isomer ^{92m}Tc was included for the sake of completeness [16].

($\mu = -0.9335\ \mu_N$) [16,44] and ^{99}Ru ($\mu = -0.641\ \mu_N$) [45]. The magnetic moment of ^{98}Tc with $I = 6$ is significantly smaller than the two other reported odd-odd isotopes ^{94,96}Tc with $I = 7$, while all three g factors are of rather similar size as shown in Fig. 6.

For the evaluation of the spectroscopic quadrupole moment Q_s, only the B coupling constants of the two upper atomic states $^6P^o_{7/2,5/2}$ were considered due to their significantly better relative accuracy. Nonetheless, the precision of the electric quadrupole moment is limited by the rather small size of these B values and the correspondingly large experimental uncertainties. For ^{97}Tc the Q_s value indicates an oblate deformation of the nucleus that is slightly larger than the one for ^{99}Tc. The small oblate deformation results from the unbound proton in a $g_{9/2}$ orbital and is similar to observations in ^{93}Nb ($Z = 41$) [46]. The paired neutrons directly above the neutron shell closure at $N = 50$ only contribute slightly to the deformation, reducing its strength with increasing number of neutrons in the nucleus. In contrast, the unbound neutron in the odd-N isotope ^{98}Tc has a clear effect on the deformation of the nucleus. Here, a small positive value of Q_s is proposed, which can be related to a small prolate deformation, close to a spherical shape.

VI. ISOTOPE SHIFTS AND MULTICONFIGURATION DIRAC-HARTREE-FOCK CALCULATIONS

From the measured spectra the center of gravity for each hyperfine structure was determined. The obtained isotope shifts with respect to the reference isotope ^{99}Tc are summarized in Table III. The quoted uncertainty is dominated by possible small changes in the angular orientation of the atom beam with respect to the laser beams, for the consecutive recording of each spectrum. The resulting error on the center-of-gravity frequency of a hyperfine structure was conservatively estimated to be 10 MHz, based on recent measurements with the experimental setup used.

TABLE III. Compilation of the isotope shifts relative to ^{99}Tc in the different transitions under study. All values are given in units of MHz.

Parameter	^{97}Tc	^{98}Tc	^{99}Tc
$\delta\nu^{99,A}$ ($^6S_{5/2}$-$^6P^o_{7/2}$)	+347(14)	+369(14)	0
$\delta\nu^{99,A}$ ($^6S_{5/2}$-$^6P^o_{5/2}$)	+313(14)	+327(14)	0
$\delta\nu^{99,A}$ ($^6S_{5/2}$-$^6P^o_{3/2}$)	+308(14)	+324(14)	0

The isotope shift of an atomic transition $\delta\nu^{A,A'} = \nu^{A'} - \nu^{A}$ between two isotopes A and A' with masses m_A and $m_{A'}$ is linked to the change in mean-square charge radii of the atomic nuclei $\delta\langle r^2\rangle^{A,A'}$ by the formula

$$\delta\nu^{A,A'} = \frac{m^{A'} - m^{A}}{m^{A'} m^{A}} M + F_s \delta\langle r^2\rangle^{A,A'}. \tag{2}$$

Thus, for the extraction of any information on the change of the size of the nucleus it is important to know the constants of the mass shift M and the field shift F_s. Because no independent measurements of the charge radii are available for a King-Plot analysis, atomic calculations employing the multiconfiguration Dirac-Hartree-Fock (MCDHF) approach were performed to extract the mass-shift and the field-shift constants of the investigated transitions [47,48].

In particular we utilized the GRASP2K code [49] to compute the isotope-shift parameters for the three transitions under consideration, as well as the hyperfine coupling constants for all four levels involved. For the computation of the mass-shift factors, the expectation value of the relativistic recoil Hamiltonian is calculated with the approximate wave functions, as implemented in the RIS3 [50] program. The field-shift factor is estimated based on a series of configuration interaction calculations [51] with varying nuclear mass and radius as detailed in Refs. [47,52]. An estimate for the uncertainty of the isotope-shift parameters is obtained by comparing results from computational models that test contributions from core correlations and different optimization strategies. For the sake of feasibility, all configurations were based initially on the two reference configurations $4d^5(5s^2 + 5p^2)$ for the ground state and on $4d^5\,5s\,5p + 4d^6\,5p$ for the excited states. The configuration space was then systematically enlarged by performing single and double excitations from the valence orbitals into several layers of virtual orbitals, which were optimized separately for every total angular symmetry. Excellent convergence is observed when extending the configuration space in this valence-valence (VV) model. In a second model calculation, core polarization effects were considered by including single excitations from all core orbitals (VV + CP model). For both models the convergence of the calculated excitation energies in different layers with increasing configuration space is summarized in Table IV. The obtained values are in good agreement within 5–13% with the experimental results for the magnetic moment and with only slightly larger discrepancy for the electric quadrupole moment. The discrepancy is significantly larger for the ground state, however, as

TABLE IV. Computed mass-shift and field-shift parameters for the three transitions under consideration using the valence-valence (VV) model and the valence-valence model including core polarization (VV + CP). For each transition the convergence for different layers L with an increasing configuration space is shown as well as the final values used for the evaluation.

	VV model			VV + CP model		
L	Energy (cm^{-1})	M (GHz/u)	F_s (GHz/fm^2)	Energy (cm^{-1})	M (GHz/u)	F_s (GHz/fm^2)
			$4d^5\,5s^2\,{}^6S_{5/2}$-$4d^5\,5s\,5p\,{}^6P^o_{3/2}$			
1	23 240	892	−1.74	21 932	622	−1.74
2	23 145	879	−1.88	21 943	731	−1.95
3	23 062	828	−1.83	21 830	701	−1.91
4	23 032	829	−1.85	21 767	697	−1.94
5	23 023	830(150)[a]	−1.84(15)[a]			
			$4d^5\,5s^2\,{}^6S_{5/2}$-$4d^5\,5s\,5p\,{}^6P^o_{5/2}$			
1	23 318	873	−1.74	21 994	626	−1.74
2	23 120	872	−1.89	21 956	748	−1.97
3	23 026	825	−1.85	21 823	721	−1.92
4	22 991	828	−1.86	21 740	724	−1.95
5	22 981	828(150)[a]	−1.85(15)[a]			
			$4d^5\,5s^2\,{}^6S_{5/2}$-$4d^5\,5s\,5p\,{}^6P^o_{7/2}$			
1	23 307	888	−1.76	22 015	675	−1.76
2	23 075	877	−1.91	21 934	799	−2.00
3	22 979	832	−1.87	21 799	771	−1.95
4	22 943	835	−1.89	21 720	776	−1.98
5	22 933	835(150)[a]	−1.88(15)[a]			

[a]Values used for the evaluation of the charge radii.

neglected core correlations play a more important role due to the closed 5s shell.

The field-shift factor F_s agrees well at a 6% level in both models, as summarized in Table IV, again including the convergence behavior for different layers. The mass-shift factor M in contrast shows a discrepancy between both models, especially for the $^6P_{3/2}$ transition. Here, the VV + CP model shows a strong variation between the transitions to different fine-structure levels. From the deviations between the two models, we estimate an uncertainty of 15%, which, unfortunately, cannot be cut down further due to computational restrictions. Due to the significantly better convergence and better agreement of the transition energies, we favor the results given by the VV model, while the remaining discrepancy between the two models serves as an estimate for the numerical uncertainty and might help to further optimize the computer codes towards a better simulation.

VII. CHARGE RADII

The calculated mass- and field-shift parameters now allow us to determine the changes in the mean-square charge radii $\delta\langle r^2\rangle$ of the Tc isotopes under investigation. The extracted $\delta\langle r^2\rangle$ values for each isotope from the three different transitions investigated agree within 8% and the averaged values result in $\delta\langle r^2\rangle^{99,98} = -0.229(35)$ fm^2 and $\delta\langle r^2\rangle^{99,97} = -0.267(35)$ fm^2. These changes in mean-square charge radii are shown in Fig. 7 in comparison to reported values for isotopes of neighboring elements. In this region the light elements from yttrium to niobium undergo a sharp increase in charge radii at $N = 60$, while this kink is smoothed in the sequence from molybdenum to heavier elements. The Tc isotopes with $N = 54$, 55, and 56 as investigated here behave similar to the isotopes of the neighboring lighter element molybdenum (Mo, $Z = 42$) with the same neutron numbers [3]. ^{98}Tc with neutron number $N = 55$ exhibits a rather large, normal odd-even staggering, which includes the change in shape as discussed above. This is consistent with the observed small, but positive quadrupole moment of ^{98}Tc in

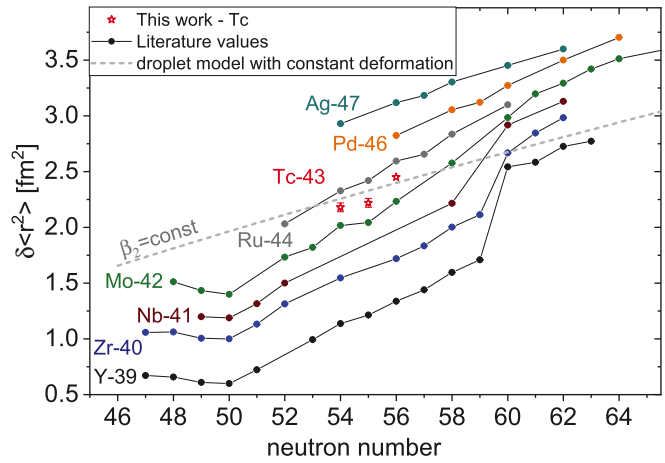

FIG. 7. Change in nuclear mean-square charge radii across the Tc region. Reference data are based on Ref. [53] with an independent offset for each element for better visibility. In addition the prediction from the droplet model [54,55] for a constant deformation is shown as a dashed line.

contrast to the larger and negative quadrupole moments for the neighboring isotopes ^{97,99}Tc. In addition to literature values also the expectation for the increase in charge radii from the droplet model [54,55] for a constant deformation is shown as a dashed line in Fig. 7. Because no deformation parameter is known for any Tc isotope, a normalization for the generation of characteristic lines for different β_2-deformation parameters is not easily possible. Nevertheless, the increase of the charge radius from ^{97}Tc to ^{99}Tc is larger than expected from the droplet model and indicates additional shape effects [47], though no change is observed for the determined quadrupole moments for ^{97,99}Tc. This can be explained by the assumption that these nuclei are not rigid and strongly deformed, but more likely would represent soft nuclear matter with a strong dynamic deformation as observed for yttrium isotopes in the same region [2].

VIII. CONCLUSION

High-resolution hyperfine structure spectroscopy on long-lived technetium isotopes allowed the determination of so far unknown nuclear ground-state properties of the isotopes ^{97,98}Tc. Three atomic transitions between the $4d^5\,5s^2\,{}^6S_5$ ground level and the low-lying $4d^5\,5s\,5p\,{}^6P_{3/2,5/2,7/2}$ levels were investigated, resulting in well-resolved spectra that allowed the precise determination of HFS coupling constants, isotope shifts, and the related nuclear parameters. From these spectra, the nuclear magnetic dipole moments for the isotopes ^{97}Tc and ^{98}Tc were determined and the predicted nuclear spin of $I = 6$ for ^{98}Tc was confirmed experimentally. In addition, an evaluation of the isotope shifts was possible by combinig the experimental results with atomic MCDHF calculations, compensating for the fact that no independent information on absolute charge radii for any technetium isotopes is available. The good agreement of the calculations in all three investigated transitions gives confidence in the results, which indicate dynamic contributions in the nuclear deformation for these isotopes located just above the $N = 50$ shell closure in agreement with observations in the vicinity.

All studies were carried out with the newly developed PI-LIST, which allows a nearly complete suppression of the dominant Doppler broadening as observed for laser spectroscopy in the conventional hot laser ion source cavity with introducing only a rather modest loss in total efficiency. The seamless integration into the existing RISIKO mass separator setup enabled the production of pure ion beams with background levels of well below 1 s^{-1}. This allowed for unrivaled laser spectroscopic off-line studies on these exotic nuclides with experimental linewidths around 100 MHz using only 10^{11} atoms despite the refractory character of technetium and the very high required source temperatures. This technical development paves the way for the investigation of further long-lived radionuclides at the RISIKO facility but also renders possible the application of the PI-LIST for direct high-resolution spectroscopy on short-lived isotopes at on-line ISOL production targets at ISOLDE and elsewhere.

ACKNOWLEDGMENTS

This work has been supported by the Bundesministerium für Bildung und Forschung (BMBF, Germany) under consecutive Projects No. 05P12UMCIA, No. 05P15UMCIA, and No, 05P18SJCIA. We thank T. Reich from the Institute of Nuclear Chemistry at the Johannes Gutenberg University Mainz for the technetium samples and we gratefully thank the IGISOL team from the University of Jyväskylä for providing the narrow-bandwidth laser stabilization hardware. P.S. acknowledges support from the BMWi (German Federal Ministry for Economic Affairs and Energy) under Contract No. 02E10981.

[1] C. Perrier and E. Segrè, J. Chem. Phys. **5**, 712 (1937).
[2] B. Cheal, M. Gardner, M. Avgoulea, J. Billowes, M. Bissell, P. Campbell, T. Eronen, K. Flanagan, D. Forest, J. Huikari, A. Jokinen, B. Marsh, I. Moore, A. Nieminen, H. Penttilä, S. Rinta-Antila, B. Tordoff, G. Tungate, and J. Äystö, Phys. Lett. B **645**, 133 (2007).
[3] F. Charlwood, K. Baczynska, J. Billowes, P. Campbell, B. Cheal, T. Eronen, D. Forest, A. Jokinen, T. Kessler, I. Moore, H. Penttilä, R. Powis, M. Rüffer, A. Saastamoinen, G. Tungate, and J. Äystö, Phys. Lett. B **674**, 23 (2009).
[4] H. Dejbakhsh, Phys. Lett. B **210**, 50 (1988).
[5] T. Thomas, K. Nomura, V. Werner, T. Ahn, N. Cooper, H. Duckwitz, M. Hinton, G. Ilie, J. Jolie, P. Petkov, and D. Radeck, Phys. Rev. C **88**, 044305 (2013).
[6] T. Thomas, V. Werner, J. Jolie, K. Nomura, T. Ahn, N. Cooper, H. Duckwitz, A. Fitzler, C. Fransen, A. Gade, M. Hinton, G. Ilie, K. Jessen, A. Linnemann, P. Petkov, N. Pietralla, and D. Radeck, Nucl. Phys. A **947**, 203 (2016).
[7] W. Bozman, C. Corliss, and J. Tech, J. Res. Natl. Bur. Stand., Sect. A **72A**, 559 (1968).
[8] P. Palmeri and J.-F. Wyart, J. Quant. Spectrosc. Radiat. Transfer **61**, 603 (1999).
[9] D. Wendlandt, J. Bauche, and P. Luc, J. Phys. B **10**, 1989 (1977).
[10] H. Walchli, R. Livingston, and W. J. Martin, Phys. Rev. **85**, 479 (1952).
[11] K. G. Kessler and R. E. Trees, Phys. Rev. **92**, 303 (1953).
[12] R. Kidd, J. Magn. Reson. **45**, 88 (1981).
[13] B. Hinfurtner, E. Hagn, E. Zech, W. Tröger, and T. Butz, Z. Phys. A **350**, 311 (1995).
[14] S. Büttgenbach, *Hyperfine Structure in 4d- and 5d-Shell Atoms* (Springer, Berlin, 1982).
[15] L. Errico, G. Darriba, M. Rentería, Z. Tang, H. Emmerich, and S. Cottenier, Phys. Rev. B **77**, 195118 (2008).
[16] N. Stone, Table of Nuclear Magnetic Dipole and Electric Quadrupole Moments, Technical Report INDC(NDS)-0658 (IAEA Nuclear Data Section, 2014).
[17] B. Singh and Z. Hu, Nucl. Data Sheets **98**, 335 (2003).
[18] S. Raeder, T. Kron, R. Heinke, J. L. Henares, N. Lecesne, P. Schönberg, M. Trümper, and K. Wendt, Hyperfine Interact. **238**, 15 (2017).

[19] N. Trautmann, Radiochim. Acta **63**, 37 (1993).

[20] K. Wendt, C. Geppert, C. Mattolat, G. Passler, S. Raeder, F. Schwellnus, K. Wies, and N. Trautmann, Anal. Bioanal. Chem. **404**, 2173 (2012).

[21] P. Schönberg, C. Mokry, J. Runke, D. Schönenbach, N. Stöbener, P. Thörle-Pospiech, N. Trautmann, and T. Reich, Anal. Chem. **89**, 9077 (2017).

[22] A. Herlert, Nucl. Phys. News **20**, 5 (2010).

[23] F. Schneider, K. Chrysalidis, H. Dorrer, C. Düllmann, K. Eberhardt, R. Haas, T. Kieck, C. Mokry, P. Naubereit, S. Schmidt, and K. Wendt, Nucl. Instrum. Methods Phys. Res., Sect. B **376**, 388 (2016).

[24] T. Kron, Y. Liu, S. Richter, F. Schneider, and K. Wendt, J. Phys. B **49**, 185003 (2016).

[25] D. Fink, S. Richter, B. Bastin, K. Blaum, R. Catherall, T. Cocolios, D. Fedorov, V. Fedosseev, K. Flanagan, L. Ghys, A. Gottberg, N. Imai, T. Kron, N. Lecesne, K. Lynch, B. Marsh, T. Mendonca, D. Pauwels, E. Rapisarda, J. Ramos, R. Rossel, S. Rothe, M. Seliverstov, M. Sjödin, T. Stora, C. V. Beveren, and K. Wendt, Nucl. Instrum. Methods Phys. Res., Sect. B **317**, 417 (2013).

[26] D. Fink, S. Richter, K. Blaum, R. Catherall, B. Crepieux, V. Fedosseev, A. Gottberg, T. Kron, B. Marsh, C. Mattolat, S. Raeder, R. Rossel, S. Rothe, F. Schwellnus, M. Seliverstov, M. Sjödin, T. Stora, P. Suominen, and K. Wendt, Nucl. Instrum. Methods Phys. Res., Sect. B **344**, 83 (2015).

[27] D. A. Fink, T. E. Cocolios, A. N. Andreyev, S. Antalic, A. E. Barzakh, B. Bastin, D. V. Fedorov, V. N. Fedosseev, K. T. Flanagan, L. Ghys *et al.*, Phys. Rev. X **5**, 011018 (2015).

[28] S. Raeder, H. Heggen, J. Lassen, F. Ames, D. Bishop, P. Bricault, P. Kunz, A. Mjøs, and A. Teigelhöfer, Rev. Sci. Instrum. **85**, 033309 (2014).

[29] R. Heinke, T. Kron, S. Raeder, T. Reich, P. Schönberg, M. Trümper, C. Weichhold, and K. Wendt, Hyperfine Interact. **238**, 6 (2017).

[30] C. Mattolat, S. Rothe, F. Schwellnus, T. Gottwald, S. Raeder, and K. Wendt, AIP Conf. Proc. **1104**, 114 (2009).

[31] S. Rothe, B. A. Marsh, C. Mattolat, V. N. Fedosseev, and K. Wendt, J. Phys.: Conf. Ser. **312**, 052020 (2011).

[32] S. Raeder, B. Bastin, M. Block, P. Creemers, P. Delahaye, R. Ferrer, X. Fléchard, S. Franchoo, L. Ghys, L. Gaffney, C. Granados, R. Heinke, L. Hijazi, M. Huyse, T. Kron, Y. Kudryavtsev, M. Laatiaoui, N. Lecesne, F. Luton, I. Moore *et al.*, Nucl. Instrum. Methods Phys. Res., Sect. B **376**, 382 (2016).

[33] V. Sonnenschein, I. D. Moore, S. Raeder, M. Reponen, H. Tomita, and K. Wendt, Laser Phys. **27**, 085701 (2017).

[34] N. Vitanov, B. Shore, L. Yatsenko, K. Böhmer, T. Halfmann, T. Rickes, and K. Bergmann, Opt. Commun. **199**, 117 (2001).

[35] R. de Groote, Modeling and simulations of two-step resonance ionization processes using CW and pulsed lasers, M.Sc. thesis, Katholieke Universiteit Leuven, 2013.

[36] V. Sonnenschein, Laser developments and high resolution resonance ionization spectroscopy of actinide elements, Ph.D. thesis, University of Jyväskylä, 2014.

[37] R. P. de Groote, M. Verlinde, V. Sonnenschein, K. T. Flanagan, I. Moore, and G. Neyens, Phys. Rev. A **95**, 032502 (2017).

[38] S. Hannemann, E.-J. van Duijn, and W. Ubachs, Rev. Sci. Instrum. **78**, 103102 (2007).

[39] M. Hori and A. Dax, Opt. Lett. **34**, 1273 (2009).

[40] A. L. Stancik and E. B. Brauns, Vib. Spectrosc. **47**, 66 (2008).

[41] S. Raeder *et al.* (unpublished).

[42] J. Persson, At. Data Nucl. Data Tables **99**, 62 (2013).

[43] H. M. Schwartz, Phys. Rev. **89**, 1293 (1953).

[44] W. G. Proctor and F. C. Yu, Phys. Rev. **81**, 20 (1951).

[45] S. Büttgenbach, R. Dicke, H. Gebauer, and M. Herschel, Z. Phys. A **280**, 217 (1977).

[46] H. Povel, Nucl. Phys. A **217**, 573 (1973).

[47] B. Cheal, T. E. Cocolios, and S. Fritzsche, Phys. Rev. A **86**, 042501 (2012).

[48] I. P. Grant, *Relativistic Quantum Theory of Atoms and Molecules: Theory and Computation*, Springer Series on Atomic, Optical, and Plasma Physics Vol. 40 (Springer Science & Business Media, New York, 2007).

[49] P. Jönsson, X. He, C. F. Fischer, and I. Grant, Comput. Phys. Commun. **177**, 597 (2007).

[50] C. Nazé, E. Gaidamauskas, G. Gaigalas, M. Godefroid, and P. Jönsson, Comput. Phys. Commun. **184**, 2187 (2013).

[51] S. Fritzsche, C. F. Fischer, and G. Gaigalas, Comput. Phys. Commun. **148**, 103 (2002).

[52] L. Filippin, R. Beerwerth, J. Ekman, S. Fritzsche, M. Godefroid, and P. Jönsson, Phys. Rev. A **94**, 062508 (2016).

[53] I. Angeli and K. Marinova, At. Data Nucl. Data Tables **99**, 69 (2013).

[54] W. D. Myers and K.-H. Schmidt, Nucl. Phys. A **410**, 61 (1983).

[55] D. Berdichevsky and F. Tondeur, Z. Phys. A **322**, 141 (1985).